Insight of the Fe Addition on the Local Structure and Electronic Properties of SrTiO3

10 AUTHORS, INCLUDING:

Lourdes Gracia
Universitat Jaume I
61 PUBLICATIONS **817** CITATIONS

SEE PROFILE

Alexandre Mesquita
São Paulo State University
39 PUBLICATIONS **151** CITATIONS

SEE PROFILE

Eduardo Antonelli
Universidade Federal de São Paulo
17 PUBLICATIONS **59** CITATIONS

SEE PROFILE

Valmor R Mastelaro
University of São Paulo
169 PUBLICATIONS **2,214** CITATIONS

SEE PROFILE

Insight into the Effects of Fe Addition on the Local Structure and Electronic Properties of SrTiO₃

Luís F. da Silva,*,† Jean-Claude M'Peko,† Juan Andrés,*,‡ Armando Beltrán,‡ Lourdes Gracia,‡ Maria I. B. Bernardi,† Alexandre Mesquita,§ Eduardo Antonelli,‖ Mário L. Moreira,⊥ and Valmor R. Mastelaro†

†Instituto de Física de São Carlos, Universidade de São Paulo, São Carlos, São Paulo 13560-970, Brazil

‡Departamento de Química Física y Analítica, Universitat Jaume I, Campus de Riu Séc, Castelló E-12080, Spain

§Universidade Estadual Paulista, UNESP, Rio Claro, São Paulo 15054-000, Brazil

‖Universidade Federal de São Paulo, UNIFESP, São José dos Campos, São Paulo 12231-280, Brazil

⊥Universidade Federal de Pelotas, Campus Universitário Capão do Leão, Pelotas, Rio Grande do Sul 96160-000, Brazil

ABSTRACT: This paper reports an experimental and theoretical investigation of the effects of adding Fe to the perovskite strontium titanate SrTiO₃. The effects include changes in the short-order range structure as well as in the electronic and electrical properties. X-ray diffraction analysis reveals that the $SrTi_{1-x}Fe_xO_3$ network shrinks with increasing Fe content, while X-ray absorption spectroscopy measurements of the Ti and Fe K-edge revealed the presence of some under-coordinated TiO_5 units created because of the partial replacement of Fe^{3+} ions in the Ti^{4+} site. UV−visible absorption spectra indicated a reduction in optical gap with increasing Fe content. The electronic structure and spin densities of STFO with x = 0, 0.0625, 0.125, 0.5, and 1 are calculated by the DFT method at the B3LYP computational level, showing a Jahn−Teller distortion of O atoms surrounding the Fe as well as the formation of under-coordinated TiO_5 units. From the electrical viewpoint, the results show that STFO is a mixed (ionic and electronic) conductor and that the electronic contribution becomes dominant with increasing Fe content.
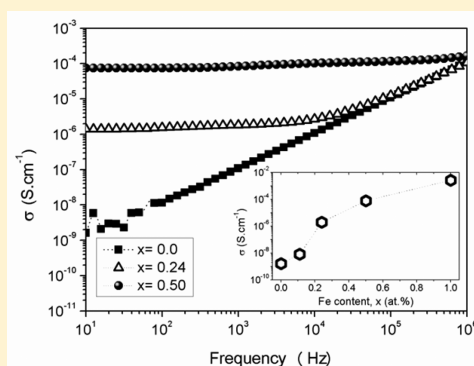
1. INTRODUCTION

Perovskites of the general formula $A^{2+}B^{4+}O^{6-}$ have attracted widespread scientific and technological interest for several decades because of their various functional properties. Its ideal structure can be described as a network of corner-linked octahedra. The smaller B-site ions occupy the corners of a cube in 6-fold oxygen coordination forming BO_6 octahedra, while the larger A-site ions are positioned in the center of the cube in AO_{12} coordination.[1] This structure is able to accommodate a large variety of atoms with different ionic radii and different valences in both the A and B sites[2−4] without destroying the original structure. Among the large family of perovskites, strontium titanate (SrTiO₃, abbreviated STO) is an important semiconductor with highly valued properties, such as high static dielectric constant and good insulation,[5,6] luminescence properties,[7,8] and usefulness as an oxygen gas sensor,[9,10] photocatalyst,[11,12] or photoelectrode.[13]

Electronic conduction in perovskites depends mainly on the crystal structure (e.g., type and number of ions, size, and symmetry and distortion of the unit cell) and the micro-structure features of the sample (usually the higher the number of grain boundaries, the lower the conductivity). This conduction occurs through the B-site network when these sites are occupied by cations capable of adopting multiple oxidation states (Ti^{4+}/Ti^{3+}, Nb^{5+}/Nb^{4+}, Mn^{4+}/Mn^{3+}, Fe^{3+}/Fe^{4+}, etc). Electrons are generated by appropriate doping and/or by exposing the materials to a reducing environment which strips oxygen ions from the structure and subsequently reduces B^{n+} to $B^{(n-1)+}$.

One well-known way to modify the electronic structure of STO to tailor its properties is through electron doping,[14,15] which can transform the intrinsically insulating STO to be metallic. Other ways include introduction of trivalent rare-earth ions in the A site (Sr site), or pentavalent transition-metal ions in the B site (Ti site), or even by introduction of oxygen vacancies. Essentially, oxygen vacancies, by introducing lattice distortions and charge carriers, show a strong impact on structural and electronic properties, such as phase transitions, ionic conductivity, and resistance switching.[16,17] STO doped with transition metals[18,19] and codoped by anion−cation pairs[20] can absorb visible light because of the gap levels introduced by the dopants to improve the photocatalytic efficiency of STO for the production of hydrogen and oxygen through water splitting.

Strontium titanate ferrite ($SrTi_{1-x}Fe_xO_3$, abbreviated STFO) solid solutions have attracted much attention for both scientific and technological consideration.[21−29] In STFO, replacing Ti^{4+} by iron as Fe^{3+} creates negatively charged defects (Fe'_{Ti}),[24,27,29−31] which are compensated by the formation of oxygen vacancies, leading to an increase in ionic conductivity.[32,33] In the case of transition metal oxides, oxygen vacancies are generally electron donors, and in STO, oxygen vacancies are particularly important because they have a tendency to retain high carrier mobilities, even at elevated carrier densities.[34]

The requirement for easy integration of this material into electronic devices makes the synthesis of high-quality STFO nanostructures interesting from both applied and fundamental standpoints. Indeed, synthetic developments must be accompanied by an in-depth understanding of the effects of the chemical composition and size on the crystal nanostructure, which ultimately determines their dielectric and optical properties. Therefore, a thorough understanding of their geometric and electronic structures is critical, and theoretical investigations may greatly contribute to the design of novel nanomaterials with enhanced performance and optimal composition.

In the past, STFO solid solutions have been prepared using a wide variety of methods.[2,25,27,35−37] Brixner was the first author to synthesize the STFO solid solutions, using the solid-state reaction procedure.[33] It is well-known that development of such reaction requires high temperatures for the sintering process (around 1200 °C) and can produce ceramic powders with chemical inhomogeneities and micrometric particles. The development of innovative chemical processing methods that allow lower preparation temperatures and improve homogeneity of compounds is highly desirable.

An alternative synthesis process, the polymeric precursor method, has been intensively used for the synthesis of several polycation oxides. The advantages of this method over the solid-state reaction procedure are a low temperature (∼700 °C) of crystallization, a high degree of control over the composition, easy reproducibility and, especially, an ability to obtain particles from nanometer to micrometer size.[7] Our research group was the first one to synthesize STFO powders with nanometer-sized particles by the polymeric precursor method.[35] In an earlier study, we described the synthesis procedure as well as the effects of Fe ions on the thermal and morphological properties of STO nanoparticles.[35] However, the effects of Fe ions on the conductance networks and the transport properties of STO nanostructures remained unclear. These effects are difficult to visualize and have not been explored by further theoretical investigations. Taking into account speculation surrounding the charge distribution and the increasing need for better control of STO conductivity, enhancing our understanding of these effects is timely and relevant.

We undertook an investigation of the role of Fe ions in the geometrical and electronic structures in STFO solid solutions, employing a variety of experimental techniques including X-ray diffraction (XRD), UV−visible absorption, X-ray absorption spectroscopy, and electrical measurements, as well as first-principles calculations aimed at getting insight into the geometric, electronic, and short-range order structural properties of these materials.

2. EXPERIMENTAL SECTION

2.1. Synthesis and Characterization Techniques.
$SrTi_{1-x}Fe_xO_3$ (STFO) powders, where $x = 0, 5, 10, 25, 50,$ 75, and 100 mol % Fe, were synthesized by the polymeric precursor method. The details regarding the synthesis procedure may be found in ref 35. The precursor powders were heat-treated in a pure alumina crucible at 750 °C, at a heating rate of 10 °C min^{-1}, for 1 h (twice) in an electric furnace under air atmosphere. Titanium and iron composition were determined by energy-dispersive X-ray analysis (SEM/EDX) in a spectrometer (Oxford, LINK ISIS300) that was coupled to the scanning electron microscope (SEM, FEI-Philips, model XL30-FEG), revealing that the Fe composition was very close to the nominal contents, as shown in Table 1.

Table 1. Rietveld Parameters Extracted from XRD Data of the STFO Samples[a]

Fe content, x (atom %)	lattice parameter, a_0 (Å)	amount of $SrCO_3$ phase (%)	χ^2	R_{WP} (%)
0.00	3.91300(4)	–	8.55	9.25
0.05	3.91157(4)	–	9.32	9.25
0.11	3.91122(4)	4.31(2)	16.98	8.89
0.24	3.91220(2)	3.20(5)	9.62	6.60
0.50	3.90600(3)	1.80(5)	17.39	8.03
0.78	3.88958(6)	6.89(8)	13.73	7.43
1.00	3.86036(3)	0.47(6)	31.27	11.99

[a]χ^2: quality of fit. R_{wp}: considered profile

STFO samples were characterized by X-ray diffraction (Rigaku, Rotaflex RU200B) with a monochromatic Cu Kα radiation source. The data were collected in the $2\theta = 20−80°$ range with a 1° divergence slit, 0.3 mm receiving slit, 0.02° step width, and 5 s point^{-1}. The structure was refined using the Rietveld method[38] and the General Structure Analysis System (GSAS) package with the EXPGUI graphical user interface.[39,40]

UV−visible spectra of STFO samples were recorded using a Cary 5G spectrometer in the total reflection mode in the 200−800 nm region. The optical gap values (E_{gap}) were estimated using the Wood and Tauc method.[41]

X-ray absorption spectroscopy (XAS) experiments were performed at the Brazilian Synchrotron Light Laboratory (LNLS), using the XAFS2 beamline. The LNLS storage ring was operated at 1.36 GeV and 160−250 mA. The Fe K-edge X-ray absorption near-edge structure (XANES) spectra were collected in transmission mode at room temperature using a Si(111) double crystal monochromator. XANES spectra at the Ti K-edge were recorded for each sample between 4950 and 5020 eV, while those for the Fe K-edge were recorded between 7050 and 7150 eV, using energy steps of 0.3 eV. For comparison purposes among the different samples, all spectra were background removed and normalized using the first extended X-ray absorption fine structure (EXAFS) oscillation as unity. The average oxidation state of iron ions was estimated from Fe K-edge XANES spectra and using the integration method.[42]

Fe K-edge EXAFS spectra were recorded between 7100 and 7900 eV with energy steps of 2 eV, whereas EXAFS spectra at the Ti K-edge were collected between 4880 and 5800 eV with energy steps of 2 eV. The EXAFS $k\chi(k)$ function was weighted with k^3 before carrying out the Fourier transform (FT). A Kaiser window ($\tau = 2.5$) was applied to the $k^3\chi(k)$-weighted data before FT. The R-range used for fitting was between 0.92 and 1.99 Å (pure STO, $x = 0.0$) and between 0.99 and 1.99 Å (STFO with $x = 0.25$). This range included only the first

nearest-neighbor shell (Ti−O bonds), and the range in k-space was 2.0−12.52 Å^{-1}. XAS spectra were processed by the multiplatform applications for XAFS code (MAX), and theoretical spectra were calculated with the ab initio FEFF8.3 code.[43,44]

The calculated Fe K-edge EXAFS spectra were obtained using, as a model, the structure based on the Rietveld refinement, with Fe atoms occupying two different sites: Ti^{4+} or Sr^{2+}. The structure model with Fe occupying the Ti^{4+} site was generated by the CRYSTALFRREV program,[44] in which the neighbors were positioned in relation to the absorbing atom as follows: 6 O atoms at 1.96 Å, 8 Sr atoms at 3.39 Å, 6 Fe/Ti atoms at 3.91 Å, 24 O atoms at 4.37 Å, 12 Fe/Ti atoms at 5.53 Å, and 29 O atoms at 5.97 Å. For the structure model with Fe atoms occupying Sr site, the neighbor atoms were positioned as follows: 12 O atoms at 2.77 Å, 8 Ti atoms at 3.39 Å, 6 Fe/Sr atoms at 3.91 Å, 24 O atoms at 4.79 Å, and 11 Fe/Ti atoms at 5.52 Å. The only fitted parameter was a global Debye−Waller factor of 0.014 Å^2 for both calculated spectra.

In addition, electrical characterization of these materials was performed to understand the role of Fe ions in the STO network. For the measurements, STFO powders were compacted into disk-shaped pellets and then sintered at 1400 °C for 2h. The final density of each sintered specimen was determined by the Archimedes' method, and the values obtained for all samples were >95% of the STO's theoretical density. The measurements were carried out with a Solartron SI 1260 impedance/gain-phase analyzer, from which conductivity data were extracted in the 10 Hz to 1 MHz frequency range, while the temperature was varied from room temperature to 200 °C. Electric contacts consisted of platinum (Pt) paste previously diffused on both parallel faces of the pellets at 700 °C for 1h.

2.2. Computational Method and Periodic Model. The calculations were carried out with the CRYSTAL09 program[45] in the framework of the density functional theory (DFT) with the hybrid functional B3LYP.[46] This scheme described Fe, Ti, Sr, and O centers as 86-411d41G, 86-411d41G, 97-641d51G, and 6-31G*, respectively. The definition of core and valence electrons for the valence basis set representing the Fe, Ti, Sr, and O centers can be found at the CRYSTAL Resources Page.[47] The diagonalization of the Fock matrix was performed at k-point grids in the reciprocal space, being the Pack−Monkhorst/Gilat shrinking factor IS = ISP = 4. The thresholds controlling the accuracy of the calculation of Coulomb and exchange integrals were set to 10^{-8} (ITOL1 to ITOL4) and 10^{-14} (ITOL5), whereas the percentage of Fock/Kohn−Sham matrices mixing was set to 40 (IPMIX = 40).[45] The band structures were obtained along the appropriate high-symmetry paths of the Brillouin zone. A note of caution is mandatory here: debate continues about the difficulty of obtaining accurate property predictions for transition metal oxides (strong correlated systems) from DFT calculations, and it is well-known that DFT underestimates the value of the band gap.[48] Despite attempts to use hybrid functional and dynamical mean field theory to treat the problem, DFT with the Becke 3-parameter (exchange), Lee−Yang−Parr (B3LYP) functional remains an appropriate choice.[49,50]

3. RESULTS AND DISCUSSION

3.1. X-ray Diffraction Measurements. X-ray diffraction patterns of the STFO powders are displayed in Figure 1. All samples were indexed as cubic perovskite structure in
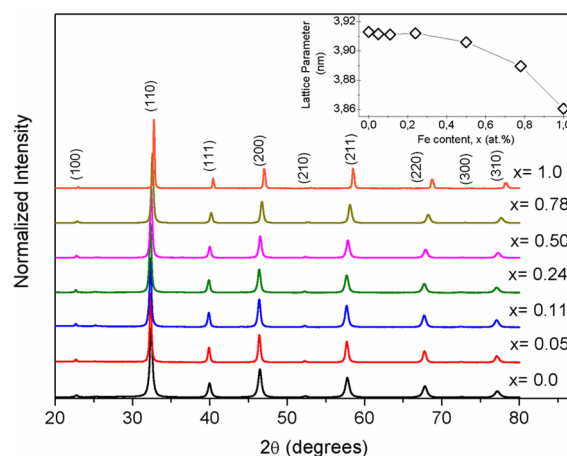

Figure 1. X-ray diffraction patterns of STFO powders. Inset shows the variation of lattice parameter with Fe content.

accordance with Joint Committee on Powder Diffraction Standards (JCPDS) Files 35-0734 and 40-0905. Some samples also presented peaks assigned to the SrCO$_3$ phase (at ∼ 25.2° and 36.2°) (JCPDS File 05-0418). Nevertheless, we did not observe any peak related to iron oxide phases, even for higher iron content. These results confirm that iron ions were incorporated homogeneously into the STO network and that solid solutions formed.

Rietveld refinements were carried out with the initial model using a cubic structure with $Pm3m$ space group for the STO phase and an orthorhombic structure with $Pmcn$ space group for the SrCO$_3$ phase. As presented in Table 1, values of R_{wp} between 11.99 and 7.43 and χ^2 between 8.55 and 31.27 were extracted from these refinements across the analyzed patterns. The values extracted for the lattice parameter a_0 and the amount of SrCO$_3$ phase are also included in this table.

The inset in Figure 1 shows the variation of the lattice parameter of the STFO samples versus Fe content. The lattice parameter a_0 varies significantly only when $x > 0.24$, noting that Vegard's law[51] was not obeyed. A similar behavior has also been observed in STFO powder samples heat-treated in an oxidant atmosphere.[27,33,52]

3.2. UV−Visible Spectroscopy Measurements. Optical absorbance measurements of the STFO samples with $x = 0.0$, 0.11, and 0.5 are shown in Figure 2. Compared to the UV−vis
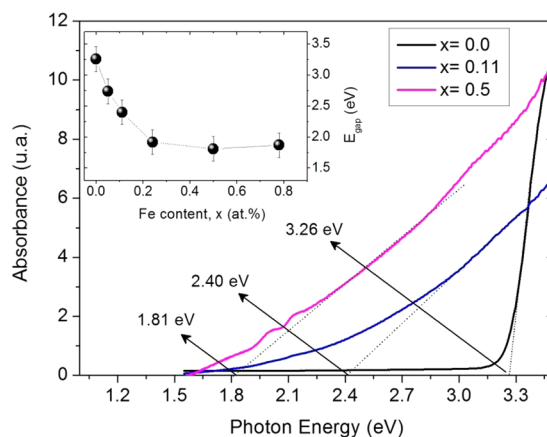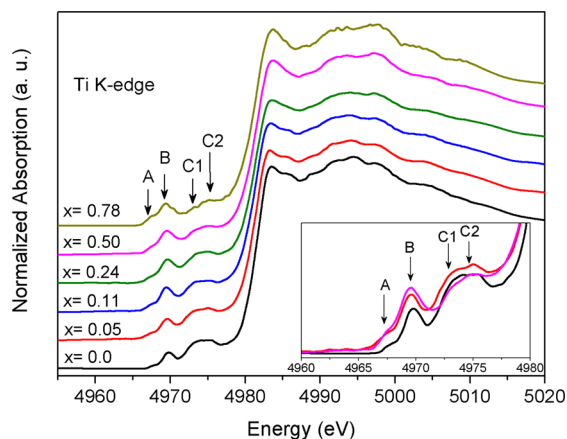

Figure 2. Absorbance spectra of STFO samples with $x = 0.0$, 0.11, and 0.5. The inset shows the optical gap (E_{gap}) with Fe content.

spectrum of an undoped STO sample, these spectra show a red-shift toward higher Fe content. Adding iron to semiconductors is an efficient way to change the band gap to the visible spectral region, a feature that is of interest for solar energy applications.[42,53,54] The inset of Figure 2 displays the optical gap (E_{gap}) values of the STFO samples obtained by the Wood and Tauc method.[41] It was not possible to estimate the E_{gap} for $SrFeO_3$ ($x = 1$) because of the high absorbance which made the UV−vis measurement infeasible.[55] E_{gap} decreases drastically from 3.2 eV (pure STO, $x = 0.0$) up to 1.9 eV (STFO with $x = 0.24$) and then shows, toward higher Fe concentrations, no significant variation. This behavior may be associated with replacement of Ti^{4+} by iron ions in the STO network, inducing the formation of a new dopant energy level below the conduction band.[54,56,57] Menesklou et al reported that the addition of Fe contributes to a broadening of the valence band of STO, which extends closer to the conduction band edge, and consequently reduces the band gap energy.[36]

3.3. X-ray Absorption Spectroscopy Measurements.
Four pre-edge transitions labeled A, B, C_1, and C_2 are observed in the Ti K-edge XANES spectra of STFO samples, as shown in Figure 3. Peak A is assigned to pure quadrupole origin due to

quantitative local structural information around Ti atoms as the amount of iron increased. The EXAFS spectra of these samples and their respective Fourier transform (FT) curves are presented in Figure 4.

Figure 4. Iron content dependence of the Ti−K EXAFS signal. (a) k^3-weighted EXAFS spectra of STFO samples with $x = 0.0$ and 0.24; (b) Fourier transform magnitude of the EXAFS spectra displayed in (a).

Figure 3. Ti K-edge XANES spectra of STFO samples. The inset shows a magnified view of the pre-edge region.
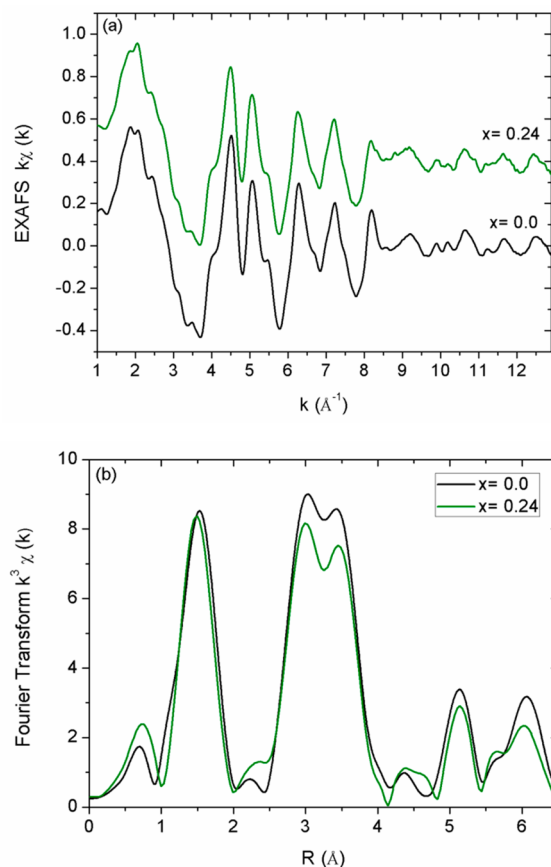
the $1s(Ti)\rightarrow 3d(t_{2g})(Ti)$ transition, whereas peak B is due to the $1s(Ti) \rightarrow 4p(Ti)$ transition, including some degree of $1s(Ti) \rightarrow 3d(e_g)(Ti)$ quadrupole contribution.[27] The overlapped peaks C_1 and C_2 are assigned to a dipole excitation of 1s electrons to t_{2g} and e_g orbitals of the neighboring TiO_6 octahedra.[27,58,59]

In recent years, our group has investigated the local structure of different amorphous and crystalline titanates, $ATiO_3$ (A = Ca, Ba, Sr) by using XANES spectroscopy.[8,60−64] In these studies, we found a relationship between the intensity of the B peak and the local symmetry of the titanium atom.[8,60−64]

As observed in Figure 3, a smaller increase in the peak B intensity and a modification in the C_1 and C_2 peaks occur as the Fe content increases. The increase in peak B intensity indicates an increased disorder on the TiO_6 units, probably due to partial replacement of Ti^{4+} by iron ions. Furthermore, the modifications in the C_1 and C_2 peaks reveal a large disturbance in the neighborhood of TiO_6 octahedra caused by the addition of Fe.[58]

Ti K-edge EXAFS spectra of two representative STFO samples, those with $x = 0.0$ and 0.24, were collected to obtain

The first FT peak (∼1.5 Å) corresponds to the first Ti−O coordination shell, whereas the subsequent FT peaks observed above 2.5 Å are related to contributions from Ti−(Sr, Ti, Fe) interactions as well as multiple-scattering effects, as shown in Figure 4b. Quantitative information about the first Ti−O coordination shell (average coordination number N, Debye−Waller factor σ^2, Ti−O mean bond length R), was obtained by considering only the first FT peak. The EXAFS spectrum of the first coordination shell was obtained by an inverse Fourier transformation. When the coordination number (N) was fixed as six and the Ti−O mean bond length and the Debye−Waller factor were varied, the fitting quality factor (QF) was not suitable. When the N parameter was also left free to vary, even for the undoped STO sample ($x = 0.0$), the QF factor was satisfactory.

According to EXAFS fitting results presented in Table 2, the replacement of Ti by Fe atoms in the STO network causes a slight reduction in the Ti−O bond length and in the coordination number. We did not observe significant change in the disorder in the Ti−O bonds, i.e., the Debye−Waller factor was not altered.

The XANES spectroscopy technique has been used to determine the oxidation state of iron in different compounds

Table 2. Structural Parameters Extracted from Ti K-Edge EXAFS Data for STFO Samples[a]

x (atom %)	N	$\sigma^2 \times 10^{-2}$ (Å)	R (Å)	ΔE_0 (eV)	QF
0.0	5.5(3)	0.7(1)	1.958(4)	3.9(9)	0.1
0.24	4.7(5)	0.6(1)	1.946(7)	3.6(9)	0.9

[a]N, first coordination shell neighbor number; σ^2, Debye–Waller factor; R, mean-length, Ti–O bond; ΔE_0, variation of the energy absorption edge in relation to the theoretical standard used in the simulation; QF, quality factor.

because of the dependence of the absorption edge position on the iron oxidation state.[65−68] We used the integration method to determine the average oxidation state value of Fe ions.[42] The pre-edge peak A observed at the Fe K-edge XANES spectra of the STFO samples and displayed in Figure 5a is related to the
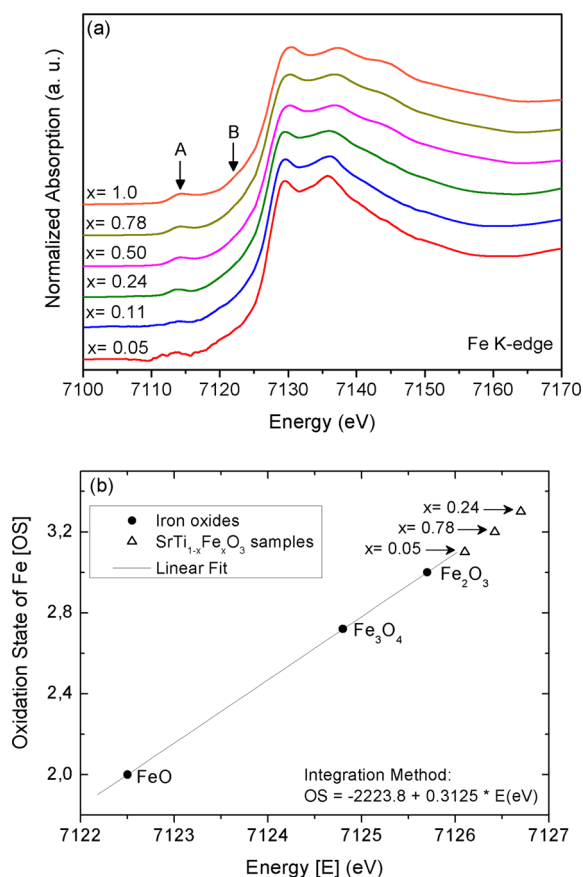

Figure 5. XANES spectra at the Fe K-edge. (a) STFO samples; (b) oxidation state of Fe^{n+} ions for STFO samples determined using integration method.[18]

$1s(Fe) \rightarrow 3d(Fe)$ quadrupole transition, while the shoulder B corresponds to pure $1s(Fe) \rightarrow 4d(Fe)$ dipole transition.[27] The Fe K-edge XANES spectra exhibit similar features, except for the samples with $x = 0.05$ and 0.11, because of the lowest iron content. The similarity among the pre-edge peaks reveals that even when the Fe content is increased, the local coordination around Fe atoms does not vary significantly.

Figure 5b shows the calibration curve and the linear equation used to determine the oxidation state of iron. The results obtained are around 3.3, indicating the coexistence of Fe^{3+} and Fe^{4+} oxidation states for all samples with a predominance of Fe^{3+} ions; the Fe^{3+}/Fe^{4+} ratio remains unchanged toward high

iron content. The presence of Fe^{3+}/Fe^{4+} ions has also been observed in STFO films and powders prepared by pulsed laser deposition[69] and the solid-state reaction procedure, respectively.[30,70]

To confirm that iron ions occupy the Ti^{4+} site in the STO network, we investigated the neighborhood around iron atoms in a STFO sample with $x = 0.24$ by comparing its experimental Fe K-edge EXAFS spectrum and the calculated EXAFS spectra. Figure 6 shows the experimental and calculated EXAFS spectra for such a sample as well as their corresponding Fourier transform curves. As can be seen in Figure 6a, the calculated EXAFS spectrum with Fe located at Sr sites is not compatible
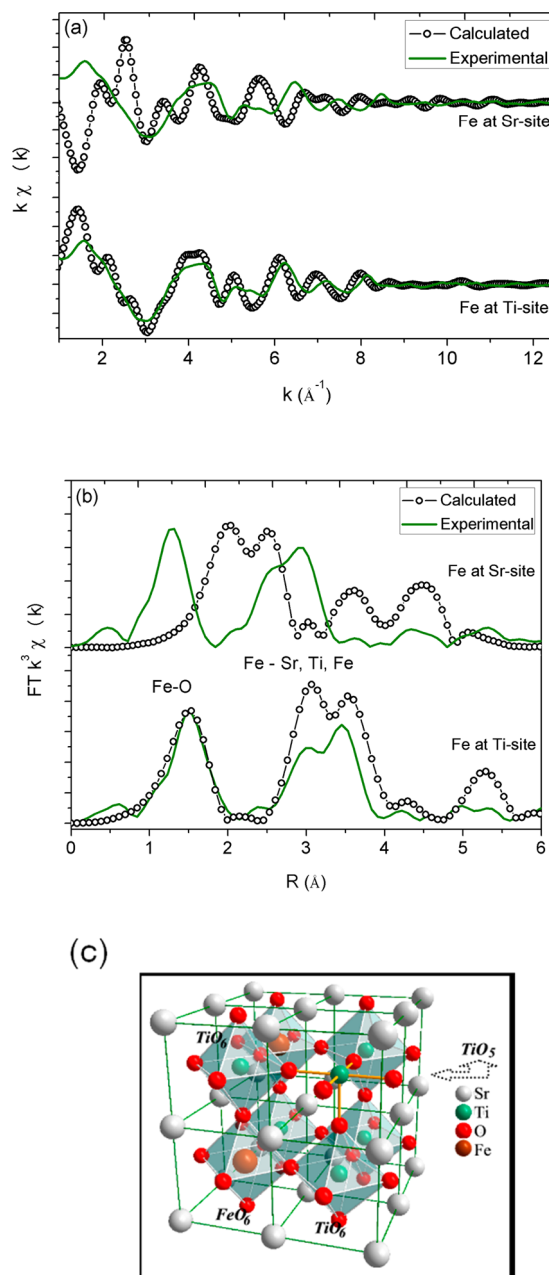

Figure 6. Experimental and calculated Fe K-edge EXAFS signals of $Sr_{0.75}Fe_{0.25}TiO_3$ and $SrTi_{0.75}Fe_{0.25}O_3$ samples (a) k^3-weighted EXAFS signals and (b) the corresponding moduli of the Fourier transforms. (c) Schematic model of the STFO crystal structure; O atoms in red, Ti atoms in green, Fe atoms in wine, and Sr atoms in gray.

with the EXAFS experimental spectrum from STFO with $x = 0.24$, whereas a good agreement is observed between the experimental EXAFS and calculated EXAFS spectra when Fe was located at the Ti site. In Figure 6b, the first two peaks of the experimental FT curve are in reasonable agreement with the calculated curve with Fe atoms located at the Ti site.

On the basis of the Fe K-edge XANES and EXAFS findings, we can state that iron occupies substitutionally the Ti^{4+} site, causing an increase in local disorder around Ti atoms mainly due to the replacement of Ti^{4+} by Fe^{3+}, which induces the development of oxygen vacancies, giving rise to some TiO_5 structural units.[24,27,28] Figure 6c shows a schematic crystalline structure of the STFO compound based on XANES and EXAFS results, where the presence of TiO_6, TiO_5−Vö complex, and FeO_6 units was considered.

3.4. Electrical Properties of STFO Samples.
Figure 7a depicts the frequency spectra of conductivity (σ) for some of
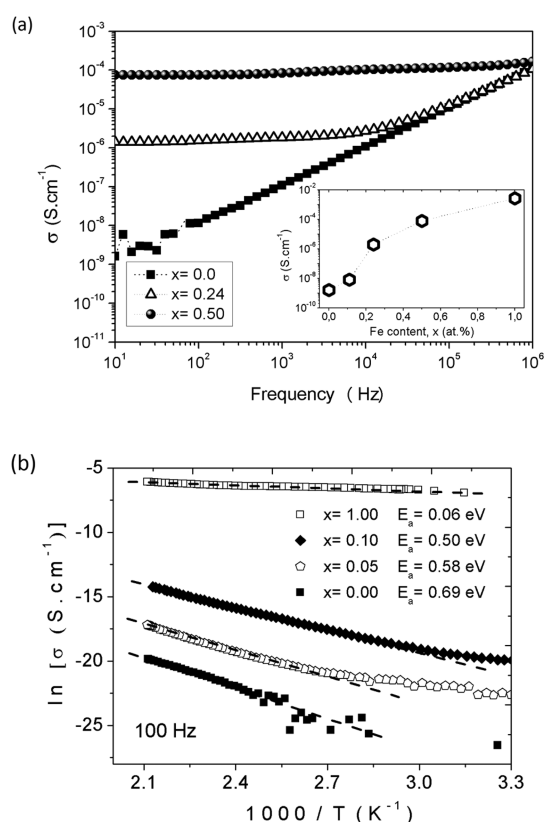
Figure 7. Electrical transport properties of some representative STFO samples: (a) frequency and (b) temperature dependences of conductivity. The inset in (a) shows the variation of conductivity with Fe content, and (b) is an Arrhenius-like graph.

the STFO samples studied in this work. The other samples were characterized by a similar behavior in the sense that, while variable toward high frequencies, the conductivity turned out to be frequency-independent at low frequencies, where direct current (dc) conduction processes may be truly assessed. This behavior conforms well to a dependence of the type $\sigma(\omega) = \sigma_{dc} + A\omega^n$, which was proposed by Jonscher as the *universal dynamic behavior* in dielectric media.[71,72] The region toward which the conductivity is dispersive ($\sigma \alpha \omega^n$) showed a constant shift toward higher frequencies with increasing Fe^{3+} content in STFO. In this work, we were interested in appraising and comparing the strength of the dc conduction processes in all

the STFO samples, the results of which are summarized in the inset of Figure 7a.

The data reveal a clear increase of conductivity as Fe ions are added to the STO network. We recall[30,73] that undoped STO is naturally a semiconductor, but with a wide band gap that exceeds 3 eV; therefore, it is characterized by low conductivities. Replacing Ti^{4+} by Fe^{3+} ions normally produces, on the one hand, a decrease in band gap to around 2 eV and, on the other hand, an increase in defect concentration, such as multivalent Fe centers, electron holes, and oxygen vacancies $(V_ö)$,[74] and the material turns out to be a mixed electronic (σ_e) and ionic (σ_i) conductor. To understand the results depicted in Figure 7a, it is worth remembering for reference that conductivity satisfies an expression of the type $\sigma = Nq\mu$, where N represents the concentration of charge carriers, q the charge value attributed to these carriers, and μ their mobility throughout the dielectric medium. From the ionic viewpoint, in terms of charge-carrier density contribution, notice that, unlike what is seen in the inset of Figure 7a, a nearly linear dependence of conductivity upon variation of Fe content would be expected. This is because an increase of Fe^{3+} ions in the STFO lattice implies a proportional rise in oxygen vacancy defects, as a self-compensated $Sr(Ti,Fe)O_{3−\delta}$-like system will in such a case form, following a reaction that can be proposed as $Fe_2O_3 \leftrightarrow 2Fe'_{Ti} + V_ö + 3O_O^X$, in which the electrical neutrality is satisfied for $[N_{Fe'_{Ti}}] = 2 [N_{V_ö}]$. Of course, the influence of the mobility term has also to be taken into account. As was shown in the inset of Figure 1, the STFO network shrinks with increasing Fe^{3+} ion content, especially for $x > 0.24$. In other words, mainly toward this composition range, the mobility of such defects and, hence, ionic conductivity would be expected to suffer a considerable reduction when Fe^{3+} ions are introduced, owing to a decrease in the free volume available for conduction.[75] Notice that this is different from the results seen in Figure 7a inset. In fact, it seems unlikely that oxygen vacancies in perovskite-structured titanate materials could lead to the relatively high room-temperature conductivity values observed in this system toward high Fe^{3+} ion concentrations. This means that a contribution from the electronic mechanism, mainly related to the presence of Fe^{3+}/Fe^{4+} defects, should be dominant in the results presented in Figure 7a for a STFO system with moderate to high Fe content.

To further approach this issue, the strength of electrical transport in these materials while varying temperature was assessed, the results of which are depicted in Figure 7b for the 100 Hz data collected from some representative STFO specimens. An Arrhenius-like graph was used, and linear behaviors are observed at high temperatures, toward which the *ac* data are predicted to reflect the results expected for the *dc* conduction processes. For the weakly doped STFO materials, this happens when the measuring frequency also becomes, with rising temperature, located within the frequency-independent conductivity plateau observed in Figure 7a.[71] This means that the high-temperature data from these materials can be fitted with a simple equation of the type $\sigma = \sigma_o \exp(-E_a/kT)$, where σ_o is the pre-exponential factor, E_a the activation energy (related to mobility), k the Boltzmann's constant, and T the absolute temperature. The following conclusions can be drawn from Figure 7b: (1) the conductivity continuously increases with temperature, a fact which excludes any metallic behavior development for the STFO materials here prepared, and (2) the activation energy (dashed lines-associated conductivity

slopes) decreases with increasing Fe content. The E_a values estimated from applying the above Arrhenius expression are directly given in the figure.

The observed results are in accordance with literature in the sense that bulk activation energies, estimated in STFO from electrical measurements, have normally been found to scale below 1 eV (i.e., below the corresponding band gap) and to sensibly reduce with rising Fe^{3+} ions in STFO, especially for $x > 0.05$.[76] Both facts are ascribed to energy states created in the band gap by the defects, giving rise to an electronic conductivity that develops together with the ionic conductivity when Fe^{3+} is added to the STO network. This statement also remains in good agreement with some electrical results from literature,[77,78] showing values of transfer number, $t = \sigma_e/(\sigma_e+\sigma_i)$, approaching unity (i.e., $\sigma_e > \sigma_i$) in STFO solid solutions with increasing dopant content. In summary, our results in Figure 7a,b reproduce well the usual picture of a composition-dependent electrical property profile in STFO in which conductivity values for $x < 0.1$ were really low (higher barrier energy) compared with the strength of conduction for $x > 0.1$ (lower barrier energy). It is timely to point out here that the reduction of the rate of conductivity increase noted in the inset of Figure 7a toward the highest STFO compositions is most likely a consequence of reduction in ionic mobility and corresponding conductivity contribution because of the aforementioned lattice shrinkage effect (Figure 1 inset). It is not clear whether probable formation of associated defects,[37] having the effect of limiting the number of charge carriers (e.g., electrons and holes) available or free for conduction, could also be contributing to this conductivity rate reduction.

3.5. First-Principles Calculations of STFO Samples. We employed the periodic supercell technique to investigate the properties of the STFO solid solutions and Fe^{4+} ions with a $3d^4$ electronic configuration. Initial calculations substituting Fe in both the Sr or Ti sites have been performed, the most stable system being that of Fe replacing Ti, in good agreement with Fe K-edge EXAFS results. For the studied STFO compositions, we explored three different spin states for each Fe^{4+} ion, i.e., high-spin (quintuplet), low-spin (triplet), and closed-shell (singlet), whereas for the STO we calculated only the singlet and the triplet states. A full optimization of the geometry was performed to determine the trends in electronic (band structure and density of states) properties of an STFO system with different Fe contents, namely, $x = 0$, 0.0625, and 1.

For $x = 0.0625$, a fcc supercell of 80 atoms was employed. The most stable spin states are singlet, triplet, and quintuplet for $x = 0$, 0.0625, and 1, respectively. A full optimization was carried out for $x = 0$, 0.0625, and 1 considering the optimized cell parameters equal to 3.8783 Å for $SrTiO_3$ ($x = 0.0$), 3.8724 Å for STFO ($x = 0.0625$), and 3.8690 Å for $SrFeO_3$ ($x = 1.0$). The theoretical calculations indicate that the presence of Fe in the STO network produces a local distortion around the Fe site. The difference in energy between triplet and quintuplet states is low: 0.13 eV. In both states we found an asymmetrical relaxation of the six nearest oxygen atoms surrounding the iron atoms due to the Jahn−Teller effect, and this was more pronounced in the quintuplet state. This finding agrees with the calculations of Blokhin and co-workers[23] and Evarestov and co-workers[17,28] performed at the PBE0 level using the same supercell to simulate the STFO system with $x = 0.0625$ and 0.125 in the high-spin Fe^{4+} state. In this spin state, they also found that full optimization reduces the symmetry from cubic to tetragonal.

The results show that in the quintuplet of STFO sample with $x = 0.0625$, the Jahn−Teller effect generates four similar distances (two of 1.870 Å and two of 1.882 Å) and two longer distances of 2.200 Å, and a slight tetragonality appears. The spin density, depicted in Figure 8, is located mainly in the Fe
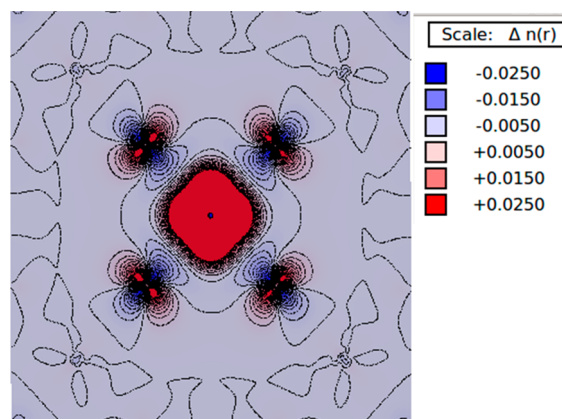

Figure 8. Spin-density map projected in a plane which contains an Fe atom and the nearest O atoms for the optimized quintuplet STFO with $x = 0.0625$.

atom (3.42), and the nearest O atoms basically complete the total spin density with residual values. The triplet state leads to the same arrangement of O atoms surrounding Fe but with slight Jahn−Teller distortion: two Fe−O distances of 1.889 Å, two of 1.901 Å, and two slightly longer distances of 1.922 Å. The spin density essentially located in the Fe atom is 1.94, and in this case the symmetry remains cubic. Note that in the centrosymmetric perovskite structure, the Fe(Ti)−O distances are equal to 1.939 Å when the lattice parameter is 3.878 Å. As a consequence of this distortion around the Fe atom, some Ti atoms manifest an under-coordination to form TiO_5 units according to Ti K-edge XAS spectroscopy measurements. The quintuplet of STFO with $x = 0.0625$ shows three TiO_5 units with five Ti−O distances in the range of 1.90−1.94 Å, and another longer distance of ∼2.0 Å. However, the triplet of STFO shows one TiO_5 unit with five Ti−O distances in the range of 1.92−1.94 Å and another longer distance of ∼1.98 Å.

The computed values of the band gap energy of the studied systems using the optimized cell parameters are the following: undoped $SrTiO_3$ presents an indirect gap from R to Γ of 3.766 eV, close to the direct gap at Γ of 3.783 eV. Pure $SrFeO_3$ tended to reveal itself to be conductor-like; however, according to the electrical results presented in Figure 7b, a nonmetallic behavior for this material is to be concluded, which is in good agreement with its mixed (ionic and electronic) conducting characteristics, as reported elsewhere.[79] Band structure and projected density of states on atoms and orbitals of the triplet of STFO with $x = 0.0625$ are shown in Figure 9a. As in the case of pure STO ($x = 0.0$), the top of the valence band is mainly formed by O 2p orbitals and the bottom of virtual bands predominantly consists of Ti 3d states. The inclusion of an Fe^{4+} impurity in the perfect crystal changes the band structure and DOS considerably. The main difference produced by the incorporation of Fe is the appearance of four localized states related to the Fe 3d levels in the interior of the band gap (near the conduction band). The β contribution to the lowest conduction band is mainly due to Fe $3d_{xz}$ states, while the upper α contribution is formed basically by Fe $3d_{x^2-y^2}$ orbitals.
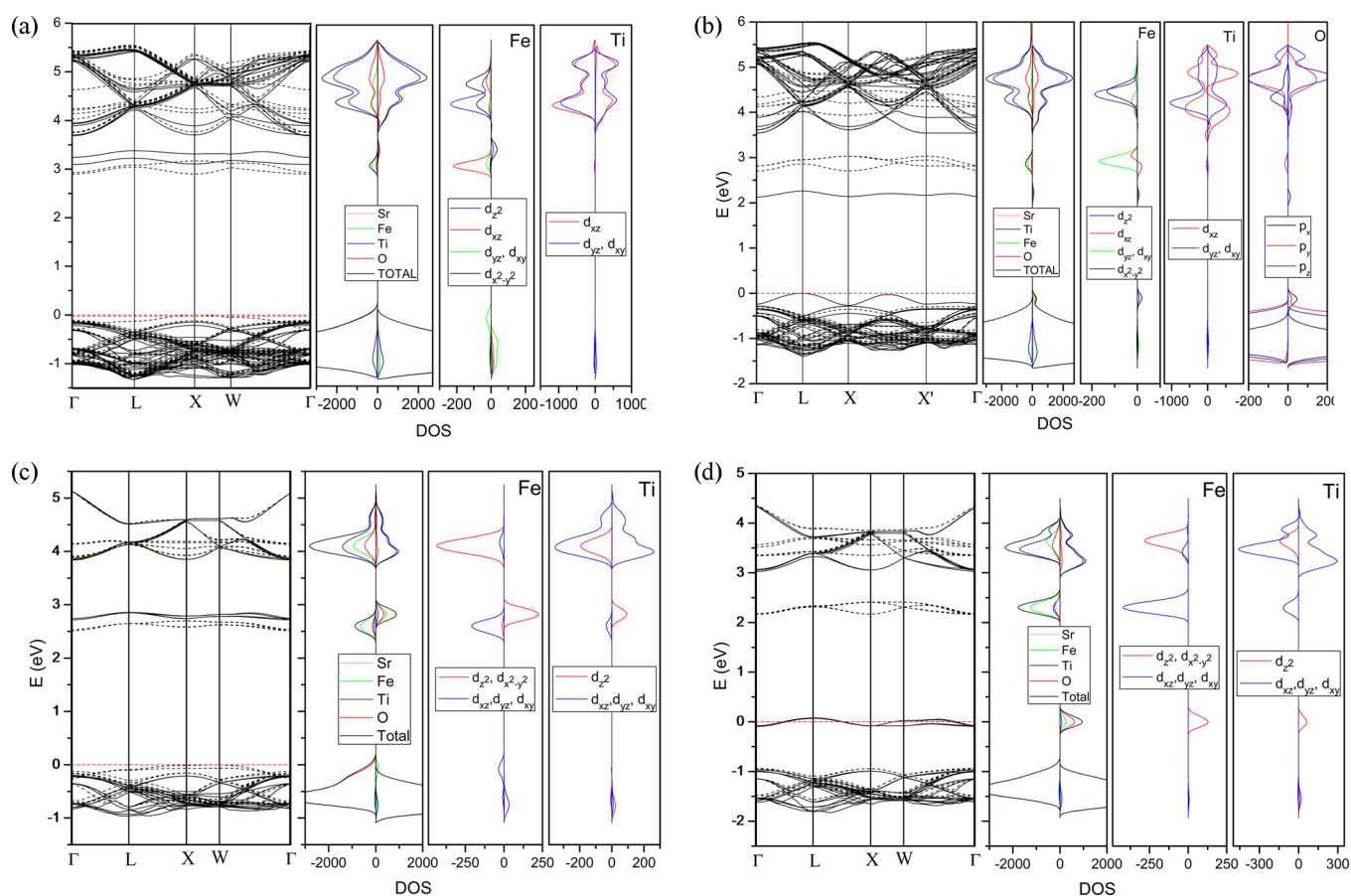
Figure 9. Band structure (α bands in solid line and β bands in dashed line) and projected density of states on atoms and orbitals of STFO for (a) $x = 0.0625$ at triplet spin state, (b) $x = 0.0625$ at quintuplet spin state, (c) $x = 0.125$ at triplet spin state, and (d) $x = 0.125$ at quintuplet spin state. The selected k points are Γ (0 0 0), L (1/2 1/2 1/2), X (1/2 0 1/2), W (1/2 1/4 3/4), X' (0 1/2 1/2).

Thus, the triplet of STFO with $x = 0.0625$ presents an indirect gap $\beta-\beta$ from X to Γ of 2.94 eV, the direct gap being at Γ of 2.99 eV, with a considerable decrease in undoped STO.

In the quintuplet of STFO with $x = 0.0625$, the incorporation of Fe also generates four localized states in the vicinity of the conduction band, but in this case the lowest of them has an α character, according to Blokhin.[23] Band structure and projected density of states on atoms and orbitals of the quintuplet of the STFO with $x = 0.0625$ are shown in Figure 9b. As in the triplet of STFO, the β contribution to the upper bands appearing near the conduction band is mainly due to Fe $3d_{xz}$ states. However, there is an indirect gap $\alpha-\alpha$ from L to Γ of 2.13 eV, with a considerable decrease in undoped STO and triplet of STFO. The α contribution to the lowest localized state near the conduction band is mainly due to O $2p_x$ orbitals and, in a minor rate, Fe $3d_{z^2}$ orbitals. The maximum of the valence band is composed by a localized state with α character formed basically by O p_x and Fe $3d_{x^2-y^2}$ contributions.

Finally, during discussion of the results arising from this study, we found it interesting to also perform some calculations for the STFO system with $x = 0.125$ and 0.5. Also in these two cases, a supercell of 80 atoms was built up for such a purpose. Accordingly, 2 of the 16 Ti atoms were substituted (by Fe) for the case of $x = 0.125$ and half of the Ti atoms (i.e., 8 atoms) for that of $x = 0.5$. Several possible Fe positions were analyzed in both cases and, for the most stable configurations we found, the electronic band structure was calculated. The results are as follows: (1) The system with $x = 0.125$ ($a = 3.9197$ Å) has an

indirect gap (β) X $\rightarrow$ Γ of 2.51 eV if the two Fe atoms are in triplet state, being the direct gap ($\alpha \rightarrow \beta$) at Γ = 2.71 eV; when the two Fe atoms are in quintuplet state, the system tended to reveal itself to be conductor-like. (2) The last observation also applied to $x = 0.5$ ($a = 3.8964$ Å) for both spin states (i.e., all 8 Fe atoms either in triplet or in quintuplet states). Band structure and projected density of states on atoms and orbitals of the triplet and quintuplet for $x = 0.125$ structure are shown in Figure 9c and 9d, respectively. As in the triplet of STFO with $x = 0.0625$, the incorporation of two Fe atoms generates four localized states in the vicinity of the conduction band, related to the Fe 3d levels. According to the electrical results presented in Figure 7b, once again, it is to be expected that these materials actually involve nonmetallic behavior or characteristics.

In summary, one of the important results of interest in the context of this study is that the electronic structure and spin densities of the STFO quintuplet calculated by the DFT method, at the B3LYP computational level, show a Jahn−Teller distortion of O atoms surrounding Fe as well as the formation of under-coordinated TiO$_5$ units. In particular, there is a decrease of the energy gap in STFO with the increase of Fe percentage (from about 3 eV to a value around 2 eV); for $x \geq 0.125$, the system is intrinsically semiconducting.

3.6. Final Remarks Applying for Future Works. It is clear that a complete structural and electronic picture of these STFO materials, including full optimization of atomic positions, presupposes achievement of further computational approach by considering a larger number of compositions. Nevertheless, this

work has presented, in a correlative fashion, the general trends observed on local structure and electronic and electrical properties caused by addition of Fe to STO. Considering the potential widespread application of such materials in electronics, including sensor devices, it would also be interesting in future works to check how external factors such as oxygen pressure, atmosphere humidity, etc., also affect the relationship between local structure and electronic and electrical properties in STFO, depending on composition. Finally, it is worth mentioning that future approaches on STFO characteristics should also consider analysis of their magnetic properties, provided that the replacement of Ti^{4+} by Fe ions generates magnetic impurities. Such an investigation is expected to allow the addressing of important issues such as whether the electrons in the magnetic impurities are localized or delocalized, whether the material is magnetic or nonmagnetic, and how strongly this fact depends on the number of Fe ions present as magnetic impurities.

4. CONCLUSIONS

In summary, a systematic experimental and theoretical investigation of the effect of Fe ions on local structure and electronic and electrical properties of STO was performed. Ti K-edge X-ray absorption spectroscopy revealed the presence of some under-coordinated TiO_5 units beyond distorted TiO_6 octahedral linkage caused by the addition of Fe. On the other hand, Fe K-edge XAS spectroscopy also showed that iron ions in STFO present a mixed Fe^{3+}/Fe^{4+} oxidation state and occupy preferentially the Ti^{4+} site. In consequence, to meet electrical neutrality, oxygen vacancies should form. Presence of both defects (i.e., Fe'_{Ti} and $V_{\ddot{o}}$) causes, first, development of under-coordinated TiO_5 units together with a decrease in STFO optical gap and, second, an increase in STFO electrical conductivity. However, the latter was revealed to be dominated by an electronic contribution toward moderate and high Fe content. This is because the estimated barrier energy decreased with increasing Fe content, moving far from 1 eV (a value toward which ionic conductivity is characteristic in such materials). Considering that the values of these barriers fell well below those corresponding to the band gap, this electronic contribution is to be ascribed to creation of energy levels within the band gap.

First-principles calculations were carried out to complement the experimental data, showing that doping with 6.25% of Fe generates a Jahn–Teller distortion of O atoms surrounding Fe as well as the formation of under-coordinated TiO_5 units. The corresponding band structure shows the appearance of four localized states related to the Fe 3d levels in the interior of the band gap near the conduction band, leading in fact to a considerable decrease of the band gap with regard to pure $SrTiO_3$. With the increase of Fe percentage to $x > 0.125$, the STFO system was shown to transit from intrinsically insulating to pseudoconducting, to be here understood as intrinsically semiconducting, in line with the conclusions derived from both the optical (UV–vis) spectroscopy and electrical measurements.

■ AUTHOR INFORMATION

Corresponding Authors
*E-mail: lfsilva83@gmail.com. Phone: +55 16 3373-9828. Fax: +55 16 3373-9824.
*E-mail: andres@qfa.uji.es. Phone: +55 16 3373-9828. Fax: +55 16 3373-9824.

Notes

■ REFERENCES

(1) Gracia, L.; Andres, J.; Longo, V. M.; Varela, J. A.; Longo, E. A Theoretical Study on the Photoluminescence of $SrTiO_3$. *Chem. Phys. Lett.* **2010**, *493* (1−3), 141−146.

(2) Jin, G.; Choi, G.; Lee, W.; Park, J. Gas Sensing Property of Perovskite $SrTi_{1−x}Fe_xO_{3−\delta}$ Fabricated by Thick Film Planar Technology. *J. Nanosci. Nanotechnol.* **2011**, *11* (2), 1738−1741.

(3) Levin, I.; Cockayne, E.; Krayzman, V.; Woicik, J. C.; Lee, S.; Randall, C. A. Local Structure of Ba(Ti,Zr)O_3 Perovskite-like Solid Solutions and Its Relation to the Band-Gap Behavior. *Phys. Rev. B* **2011**, *83* (9), 094122.

(4) Mesquita, A.; Mastelaro, V. R.; Michalowicz, A. In Situ X-ray Diffraction Studies of Phase Transition in $Pb_{1−x}La_xZr_{0.40}Ti_{0.60}O_3$ Ferroelectric Ceramics. *Phase Transitions* **2010**, *83* (4), 251−262.

(5) Jia, C. L.; Urban, K.; Hoffmann, S.; Waser, R. Microstructure of Columnar-Grained $SrTiO_3$ and $BaTiO_3$ Thin Films Prepared by Chemical Solution Deposition. *J. Mater. Res.* **1998**, *13* (8), 2206−2217.

(6) Haeni, J. H.; Irvin, P.; Chang, W.; Uecker, R.; Reiche, P.; Li, Y. L.; Choudhury, S.; Tian, W.; Hawley, M. E.; Craigo, B.; Tagantsev, A. K.; Pan, X. Q.; Streiffer, S. K.; Chen, L. Q.; Kirchoefer, S. W.; Levy, J.; Schlom, D. G. Room-Temperature Ferroelectricity in Strained $SrTiO_3$. *Nature* **2004**, *430* (7001), 758−761.

(7) da Silva, L. F.; Maia, L. J. Q.; Bernardi, M. I. B.; Andres, J. A.; Mastelaro, V. R. An Improved Method for Preparation of $SrTiO_3$ Nanoparticles. *Mater. Chem. Phys.* **2011**, *125* (1−2), 168−173.

(8) Longo, V. M.; de Figueiredo, A. T.; de Lazaro, S.; Gurgel, M. F.; Costa, M. G. S.; Paiva-Santos, C. O.; Varela, J. A.; Longo, E.; Mastelaro, V. R.; De Vicente, F. S.; Hernandes, A. C.; Franco, R. W. A. Structural Conditions that Leads to Photoluminescence Emission in $SrTiO_3$: An Experimental and Theoretical Approach. *J. Appl. Phys.* **2008**, *104* (2), 023515.

(9) Hara, T.; Ishiguro, T. Oxygen Sensitivity of $SrTiO_3$ Thin Film Prepared Using Atomic Layer Deposition. *Sens. Actuators, B* **2009**, *136* (2), 489−493.

(10) Choi, S. H.; Choi, S. J.; Min, B. K.; Lee, W. Y.; Park, J. S.; Kim, I. D. Facile Synthesis of p-type Perovskite $SrTi_{0.65}Fe_{0.35}O_{3−\delta}$ Nanofibers Prepared by Electrospinning and Their Oxygen-Sensing Properties. *Macromol. Mater. Eng.* **2013**, *298* (5), 521−527.

(11) da Silva, L. F.; Avansi, W.; Andres, J.; Ribeiro, C.; Moreira, M. L.; Longo, E.; Mastelaro, V. R. Long-Range and Short-Range Structures of Cube-like Shape $SrTiO_3$ Powders: Microwave-Assisted Hydrothermal Synthesis and Photocatalytic Activity. *Phys. Chem. Chem. Phys.* **2013**, *15* (29), 12386−12393.

(12) Dong, W.; Li, X.; Yu, J.; Guo, W.; Li, B.; Tan, L.; Li, C.; Shi, J.; Wang, G. Porous $SrTiO_3$ Spheres with Enhanced Photocatalytic Performance. *Mater. Lett.* **2012**, *67* (1), 131−134.

(13) Jin, K. X.; Li, Y. F.; Wang, Z. L.; Peng, H. Y.; Lin, W. N.; Kyaw, A. K. K.; Jin, Y. L.; Jin, K. J.; Sun, X. W.; Soci, C.; Wu, T. Tunable Photovoltaic Effect and Solar Cell Performance of Self-Doped Perovskite $SrTiO_3$. *AIP Adv.* **2012**, *2* (4).

(14) Schultz, M.; Klein, L. Relaxation of Transport Properties in Electron-Doped SrTiO$_3$. *Appl. Phys. Lett.* **2007**, *91* (15), 151104.

(15) Leitner, A.; Rogers, C. T.; Price, J. C.; Rudman, D. A.; Herman, D. R. Pulsed Laser Deposition of Superconducting Nb-doped Strontium Titanate Thin Films. *Appl. Phys. Lett.* **1998**, *72* (23), 3065.

(16) Buban, J. P.; Iddir, H.; Ogut, S. Structural and Electronic Properties of Oxygen Vacancies in Cubic and Antiferrodistortive phases of SrTiO$_3$. *Phys. Rev. B* **2004**, *69* (18), 180102.

(17) Szot, K.; Speier, W.; Bihlmayer, G.; Waser, R. Switching the Electrical Resistance of Individual Dislocations in Single-Crystalline SrTiO$_3$. *Nat. Mater.* **2006**, *5* (4), 312−320.

(18) Konta, R.; Ishii, T.; Kato, H.; Kudo, A. Photocatalytic Activities of Noble Metal Ion Doped SrTiO$_3$ under Visible Light Irradiation. *J. Phys. Chem. B* **2004**, *108* (26), 8992−8995.

(19) Wang, D.; Ye, J.; Kako, T.; Kimura, T. Photophysical and Photocatalytic Properties of SrTiO$_3$ Doped with Cr Cations on Different Sites. *J. Phys. Chem. B* **2006**, *110* (32), 15824−15830.

(20) Shi, W. J.; Xiong, S. J. Ab Initio Study on Band-Gap Narrowing in SrTiO$_3$ with Nb-C-Nb codoping. *Phys. Rev. B* **2011**, *84* (20), 205210.

(21) Mastelaro, V. R.; Zílio, S. C.; da Silva, L. F.; Pelissari, P. I.; Bernardi, M. I. B.; Guerin, J.; Aguir, K. Ozone Gas Sensor Based on Nanocrystalline SrTi$_{1−x}$Fe$_x$O$_3$ Thin Films. *Sens. Actuators, B* **2013**, *181* (0), 919−924.

(22) Alexandrov, V. E.; Maier, J.; Evarestov, R. A. Ab Initio Study of SrFe$_x$Ti$_{1−x}$O$_3$: Jahn-Teller Distortion and Electronic Structure. *Phys. Rev. B* **2008**, *77* (7), 075111.

(23) Blokhin, E.; Kotomin, E. A.; Maier, J. First-Principles Phonon Calculations of Fe^{4+} Impurity in SrTiO$_3$. *J. Phys.: Condens. Matter* **2012**, *24* (10), 104024.

(24) Blokhin, E.; Kotomin, E.; Kuzmin, A.; Purans, J.; Evarestov, R.; Maier, J. Theoretical Modeling of the Complexes of Iron Impurities and Oxygen Vacancies in SrTiO$_3$. *Appl. Phys. Lett.* **2013**, *102* (11), 112913.

(25) Neri, G.; Micali, G.; Bonavita, A.; Licheri, R.; Orru, R.; Cao, G.; Marzorati, D.; Borla, E. M.; Roncari, E.; Sanson, A. FeSrTiO$_3$-Based Resistive Oxygen Sensors for Application in Diesel Engines. *Sens. Actuators, B* **2008**, *134* (2), 647−653.

(26) Jiang, P.; Bi, L.; Sun, X.; Kim, D. H.; Jiang, D.; Wu, G.; Dionne, G. F.; Ross, C. A. The Effect of A-site Substitution of Ce and La on the Magnetic and Electronic Properties of Sr(Ti$_{0.6}$Fe$_{0.4}$)O$_{(3−\delta)}$ Films. *Inorg. Chem.* **2012**, *51* (24), 13245−13253.

(27) Vracar, M.; Kuzmin, A.; Merkle, R.; Purans, J.; Kotomin, E. A.; Maier, J.; Mathon, O. Jahn-Teller Distortion around Fe^{4+} in Sr(Fe$_x$Ti$_{1−x}$)O$_{3−\delta}$ from X-ray Absorption Spectroscopy, X-ray Diffraction, and Vibrational Spectroscopy. *Phys. Rev. B* **2007**, *76* (17), 174107.

(28) Evarestov, R.; Blokhin, E.; Gryaznov, D.; Kotomin, E. A.; Merkle, R.; Maier, J. Jahn-Teller Effect in the Phonon Properties of Defective SrTiO$_3$ from First Principles. *Phys. Rev. B* **2012**, *85* (17), 174303.

(29) Ghaffari, M.; Shannon, M.; Hui, H.; Tan, O. K.; Irannejad, A. Preparation, Surface State and Band Structure Studies of SrTi$_{(1−x)}$Fe$_{(x)}$O$_{(3−\delta)}$ (x = 0−1) Perovskite-type Nano Structure by X-ray and Ultraviolet Photoelectron Spectroscopy. *Surf. Sci.* **2012**, *606* (5−6), 670−677.

(30) Rothschild, A.; Menesklou, W.; Tuller, H. L.; Ivers-Tiffee, E. Electronic Structure, Defect Chemistry, and Transport Properties of SrTi$_{1−x}$Fe$_x$O$_{3−y}$ Solid Solutions. *Chem. Mater.* **2006**, *18* (16), 3651−3659.

(31) Dulov, E. N.; Ivoilov, N. G.; Strebkov, O. A.; Tagirov, L. R.; Nuzhdin, V. I.; Khaibullin, R. I.; Kazan, S.; Mikailzade, F. A. Magnetic Phase Composition of Strontium Titanate Implanted with Iron. *Mater. Res. Bull.* **2011**, *46* (12), 2304−2307.

(32) Meuffels, P. Propane Gas Sensing with High-Density SrTi$_{0.6}$Fe$_{0.4}$O$_{(3−\delta)}$ Ceramics Evaluated by Thermogravimetric Analysis. *J. Eur. Ceram. Soc.* **2007**, *27* (1), 285−290.

(33) Brixner, L. H. Preparation and Properties of the SrTi$_{1−x}$Fe$_x$O$_{3−x/2}\varnothing_{x/2}$. *Mater. Res. Bull.* **1968**, *3* (4), 299−308.

(34) Tufte, O. N.; Chapman, P. W. Electron Mobility in Semiconducting Strontium Titanate. *Phys. Rev.* **1967**, *155* (3), 796−802.

(35) da Silva, L. F.; Bernardi, M. I. B.; Maia, L. J. Q.; Frigo, G. J. M.; Mastelaro, V. R. Synthesis and Thermal Decomposition of SrTi$_{1−x}$Fe$_x$O$_3$ (0.0 ≤ x ≤ 0.1) Powders Obtained by the Polymeric Precursor Method. *J. Therm. Anal. Calorim.* **2009**, *97* (1), 173−177.

(36) Rothschild, A.; Litzelman, S. J.; Tuller, H. L.; Menesklou, W.; Schneider, T.; Ivers-Tiffee, E. Temperature-Independent Resistive Oxygen Sensors Based on SrTi$_{1−x}$Fe$_x$O$_{3−\delta}$ Solid Solutions. *Sens. Actuators, B* **2005**, *108* (1−2), 223−230.

(37) Steinsvik, S.; Bugge, R.; Gjonnes, J.; Tafto, J.; Norby, T. The Defect Structure of SrTi$_{1−x}$Fe$_x$O$_{3−y}$ (x = 0−0.8) Investigated by Electrical Conductivity Measurements and Electron Energy Loss Spectroscopy (EELS). *J. Phys. Chem. Solids* **1997**, *58* (6), 969−976.

(38) Rietveld, H. M. A Profile Refinement Method for Nuclear and Magnetic Structures. *J. Appl. Crystallogr.* **1969**, *2*, 65−71.

(39) Larson, A. C.; Von Dreele, R. B. General Structure Analysis System (GSAS). LAUR 86-748 *Los Alamos National Laboratory Report.* 1994.

(40) Toby, B. H. EXPEGUI, A Graphical User Interface for GSAS. *J. Appl. Crystallogr.* **2001**, *34*, 210−213.

(41) Wood, D. L.; Tauc, J. Weak Absorption Tails in Amorphous Semiconductors. *Phys. Rev. B* **1972**, *5* (8), 3144−3151.

(42) Olimov, K.; Falk, M.; Buse, K.; Woike, T.; Hormes, J.; Modrow, H. X-ray Absorption Near Edge Spectroscopy Investigations of Valency and Lattice Occupation Site of Fe in Highly Iron-Doped Lithium Niobate Crystals. *J. Phys.: Condens. Matter* **2006**, *18* (22), 5135−5146.

(43) Ankudinov, A. L.; Ravel, B.; Rehr, J. J.; Conradson, S. D. Real-Space Multiple-Scattering Calculation and Interpretation of X-ray Absorption Near-Edge Structure. *Phys. Rev. B* **1998**, *58* (12), 7565−7576.

(44) Michalowicz, A.; Moscovici, J.; Muller-Bouvet, D.; Provost, K. MAX: Multiplatform Applications for XAFS. In *14th International Conference on X-Ray Absorption Fine Structure*, DiCicco, A.; Filipponi, A., Eds. Iop Publishing Ltd: Bristol, 2009; Vol. 190.

(45) Dovesi, R.; Saunders, V. R.; Roetti, C.; Orlando, R.; Zicovich-Wilson, C. M.; Civalleri, B.; Pascale, F.; Doll, K.; Harrison, N. M.; Bush, I. J.; Arco, P. D.; Llunell, M. CRYSTAL09; University of Torino: Torino, Italy, 2009

(46) Becke, A. D. Density-Functional Thermochemistry. III. The Role of Exact Exchange. *J. Chem. Phys.* **1993**, *98* (7), 5648−5652.

(47) Towler, M. CRYSTAL Resources Page. http://www.tcm.phy.cam.ac.uk/~mdt26/crystal.html.

(48) Ekuma, C. E.; Bagayoko, D. Ab-initio Electronic and Structural Properties of Rutile Titanium Dioxide. *Jpn. J. Appl. Phys.* **2011**, *50* (0), 101103.

(49) Fujishima, A.; Zhang, X.; Tryk, D. A. TiO$_2$ Photocatalysis and Related Surface Phenomena. *Surf. Sci. Rep.* **2008**, *63* (12), 515−582.

(50) Jeong, W. -J.; Moon, I. -S.; Cho, S. -K.; Yang, H. -H.; Park, G. -C.; Gu, H. -B.; Kim, K. -J.; Ahn, H. -G. Visible Light-Responsive Titanium Dioxide Thin Film Prepared by Reactive Sputtering. *J. Nanosci. Nanotechnol.* **2011**, *11*, 1565−1568.

(51) Denton, A. R.; Ashcroft, N. W. Vegard's Law. *Phys. Rev. A* **1991**, *43* (6), 3161−3164.

(52) Clevenger, T. R. Effect of Fe^{4+} in the System SrFeO$_3$-SrTiO$_3$. *J. Am. Ceram. Soc.* **1963**, *46* (5), 207−210.

(53) Choi, W. Y.; Termin, A.; Hoffmann, M. R. The role of Metal Ion Dopants in Quantum-Sized TiO$_2$: Correlation between Photoreactivity and Charge Carrier Recombination Dynamics. *J. Phys. Chem.* **1994**, *98* (51), 13669−13679.

(54) Liu, X. W.; Devaraju, M. K.; Yin, S.; Sumiyoshi, A.; Kumei, T.; Nishimoto, K.; Sato, T. The Preparation and Characterization of Tabular, Pearlescent Fe-Doped Potassium Lithium Titanate. *Dyes Pigm.* **2010**, *84* (3), 237−241.

(55) Ghaffari, M.; Huang, H.; Tan, O. K.; Shannon, M. Band Gap Measurement of SrFeO$_{3−\delta}$ by Ultraviolet Photoelectron Spectroscopy and Photovoltage Method. *CrystEngComm* **2012**, *14* (21), 7487−7492.

(56) Castro-Lopez, C. A.; Centeno, A.; Giraldo, S. A. Fe-Modified TiO$_2$ Photocatalysts for the Oxidative Degradation of Recalcitrant Water Contaminants. *Catal. Today* **2010**, *157* (1−4), 119−124.

(57) Zhang, K. Z.; Lin, B. Z.; Chen, Y. L.; Xu, B. H.; Pian, X. T.; Kuang, J. D.; Li, B. Fe-Doped and ZnO-Pillared Titanates as Visible-Light-Driven Photocatalysts. *J. Colloid Interface Sci.* **2011**, *358* (2), 360−368.

(58) Krayzman, V.; Levin, I.; Woicik, J. C.; Yoder, D.; Fischer, D. A. Effects of Local Atomic Order on the Pre-Edge Structure in the Ti *K* X-ray Absorption Spectra of Perovskite CaTi$_{1-x}$Zr$_x$O$_3$. *Phys. Rev. B* **2006**, *74* (22), 224104.

(59) Vedrinskii, R. V.; Kraizman, V. L.; Novakovich, A. A.; Demekhin, P. V.; Urazhdin, S. V. Pre-Edge Fine Structure of the 3d Atom K X-ray Absorption Spectra and Quantitative Atomic Structure Determinations for Ferroelectric Perovskite Structure Crystals. *J. Phys.: Condens. Matter* **1998**, *10* (42), 9561−9580.

(60) da Silva, L. F.; Avansi, W.; Moreira, M. L.; Mesquita, A.; Maia, L. J. Q.; Andres, J.; Longo, E.; Mastelaro, V. R. Relationship between Crystal-Shape, Photoluminescence, and Local Structure in SrTiO$_3$ Synthesized by Microwave-Assisted Hydrothermal Method. *J. Nanomater.* **2012**, *2012* (0), 890397.

(61) de Lazaro, S.; Milanez, J.; de Figueiredo, A. T.; Longo, V. M.; Mastelaro, V. R.; De Vicente, F. S.; Hernandes, A. C.; Varela, J. A.; Longo, E. Relation between Photoluminescence Emission and Local Order-Disorder in the CaTiO$_3$ Lattice Modifier. *Appl. Phys. Lett.* **2007**, *90* (11), 111904.

(62) Moreira, M. L.; Mambrini, G. P.; Volanti, D. P.; Leite, E. R.; Orlandi, M. O.; Pizani, P. S.; Mastelaro, V. R.; Paiva-Santos, C. O.; Longo, E.; Varela, J. A. Hydrothermal Microwave: A New Route to Obtain Photoluminescent Crystalline BaTiO$_3$ Nanoparticles. *Chem. Mater.* **2008**, *20* (16), 5381−5387.

(63) Moreira, M. L.; Longo, V. M.; Avansi, W., Jr; Ferrer, M. M.; Andres, J.; Mastelaro, V. R.; Varela, J. A.; Longo, E. Quantum Mechanics Insight into the Microwave Nucleation of SrTiO$_3$ Nanospheres. *J. Phys. Chem. C* **2012**, *116* (46), 24792−24808.

(64) Moreira, M. L.; Paris, E. C.; do Nascimento, G. S.; Longo, V. M.; Sambrano, J. R.; Mastelaro, V. R.; Bernardi, M. I. B.; Andres, J.; Varela, J. A.; Longo, E. Structural and Optical Properties of CaTiO$_3$ Perovskite-Based Materials Obtained by Microwave-Assisted Hydrothermal Synthesis: An Experimental and Theoretical Insight. *Acta Mater.* **2009**, *57* (17), 5174−5185.

(65) Bajt, S.; Sutton, S. R.; Delaney, J. S. X-ray Microprobe Analysis of Iron Oxidation-States in Silicates and Oxides using X-ray Absorption Near-Edge Structure. *Geochim. Cosmochim. Acta* **1994**, *58* (23), 5209−5214.

(66) Wilke, M.; Partzsch, G. M.; Bernhardt, R.; Lattard, D. Determination of the Iron Oxidation State in Balsatic Glasses using XANES at the K-Edge. *Chem. Geol.* **2005**, *220* (1−2), 141.

(67) Requejo, F. G.; Ramallo-Lopez, J. M.; Beltramone, A. R.; Pierella, L. B.; Anunziata, O. A. Fe-Containing ZSM-11 Zeolites as Active Catalyst for SCR of NO$_x$: Part II. XAFS Characterization and its Relationship with the Catalytic Properties. *Appl. Catal., A* **2004**, *266* (2), 147−153.

(68) da Silva, L. F.; Avansi, W.; Moreira, M. L.; Andres, J.; Longo, E.; Mastelaro, V. R. Novel SrTi$_{1-x}$Fe$_x$O$_3$ Nanocubes Synthesized by Microwave-Assisted Hydrothermal Method. *CrystEngComm* **2012**, *14* (11), 4068−4073.

(69) Kim, D. H.; Aimon, N. M.; Bi, L.; Florez, J. M.; Dionne, G. F.; Ross, C. A. Magnetostriction in Epitaxial SrTi$_{1-x}$Fe$_x$O$_3$ Perovskite Films with *x* = 0.13 and 0.35. *J. Phys.: Condens. Matter* **2013**, *25* (2), 026002.

(70) Ghaffari, M.; Liu, T.; Huang, H.; Tan, O. K.; Shannon, M. Investigation of Local Structure Effect and X-ray Absorption Characteristics (EXAFS) of Fe(Ti) K-edge on Photocatalyst Properties of SrTi$_{(1-x)}$Fe$_{(x)}$O$_{(3-\delta)}$. *Mater. Chem. Phys.* **2012**, *136* (2−3), 347−357.

(71) M'Peko, J. C. Dynamics of the Electrical Response of Ceramic Dielectric Materials in the Presence of Interfacial Blocking Effects. *J. Mater. Sci. Lett.* **2000**, *19* (21), 1925−1927.

(72) Jonscher, A. K. *Dielectric Relaxation in Solids*; Chelsea Dielectrics Press Ltd: U.K., 1983; Vol. 1, p 396.

(73) Choi, G. M.; Tuller, H. L.; Goldschmidt, D. Electronic-Transport Behavior in Single-Crystalline Ba$_{0.03}$Sr$_{0.97}$TiO$_3$. *Phys. Rev. B* **1986**, *34* (10), 6972−6979.

(74) Drahus, M. D.; Jakes, P.; Erdem, E.; Eichel, R. A. Defect Structure of the Mixed Ionic−Electronic Conducting Sr[Ti,Fe]O$_x$ Solid-Solution System — Change in Iron Oxidation States and Defect Complexation. *Solid State Ionics* **2011**, *184* (1), 47−51.

(75) M'Peko, J. C.; Paz, F. Y.; Mir, M.; De Souza, M. F. Electromigration an Charge Carrier Density versus Free Lattice Volume Effects in Doped Zirconia Ceramics. *Phys. Status Solidi B* **2004**, *241* (13), 2898−2904.

(76) Jung, W.; Tuller, H. L. Impedance Study of SrTi$_{1-x}$Fe$_x$O$_{3-\delta}$ (*x* = 0.05 to 0.80) Mixed Ionic-Electronic Conducting Model Cathode. *Solid State Ionics* **2009**, *180* (11−13), 843−847.

(77) Jurado, J. R.; Colomer, M. T.; Frade, J. R. Impedance Spectroscopy of Sr$_{0.97}$Ti$_{1-x}$Fe$_x$O$_{3-\delta}$ Materials with Moderate Fe-Contents. *Solid State Ionics* **2001**, *143* (2), 251−257.

(78) Jurado, J. R.; Colomer, M. T.; Frade, J. R. Electrical Characterization Sr$_{0.97}$Ti$_{1-x}$Fe$_x$O$_{3-\delta}$ by Complex Impedance. *J. Am. Ceram. Soc.* **2000**, *83* (11), 2715−2720.

(79) Post, M. L.; Sanders, B. W.; Kennepohl, P. Thin Films of Non-Stoichiometric Perovskites as Potential Oxygen Sensors. *Sens. Actuators, B* **1993**, *13* (1−3), 272−275.